3D Near-Surface Shear-Wave Velocity Structure from Ambient-Noise Tomography and Borehole Data in the Hefei Urban Area, China

by Cheng Li, Huajian Yao, Hongjian Fang, Xianliang Huang, Kesong Wan, Haijiang Zhang, and Kangdong Wang

ABSTRACT

Imaging near-surface structure with active sources, such as dynamite or vibrators, is usually difficult in urban areas because of dense population and safety issues. However, ambient-noise tomography can provide an alternative way to investigate near-surface structures without such difficulties. Here, we conduct ambient-noise tomography to investigate the near-surface shear-velocity structure in the urban area of the city of Hefei (about a 5 km × 7 km region) in eastern China, using two weeks of continuous ambient-noise data. The direct surface-wave tomographic method with period-dependent raytracing is used to invert all surface-wave dispersion data in the period band 0.5–2 s simultaneously for 3D variations of shear-velocity structures. To constrain the top 30-m velocity structure in the inversion, we utilize the borehole data in the city of Hefei to obtain a better 3D reference wavespeed model in the top 30 m. Our tomographic results from surface to about 400 m depth suggest that the northern part of the urban region presents higher shear velocity than the southern part. This result is consistent with regional geology; that is, the southern part of the study region is closer to Chao Lake, the fifth largest freshwater lake in China, which has much thicker sediments and lower shear wavespeed. The sharp velocity variation in our obtained model matches the location of the Shushan fault, which is associated with large gravity variations. Our near-surface velocity model of the Hefei urban area provides useful information for city planning as well as for earthquake strong ground motion prediction, which may bring strong engineering interests in the future.

Online Material: Figures showing inversion of *S*-wave velocity results.

INTRODUCTION

The Hefei basin (HFB) (Fig. 1a) is located in eastern China. The city of Hefei is on the north edge of the basin and is the capital city of Anhui province, with a population of ~4 million residents in the urban area. The Dabie orogenic zone in the west of the HFB and the Tanlu fault (TLF) (Fig. 1a) in the east provide the major tectonic forces for the basin formation and evolution (Ding *et al.*, 2002). Generally speaking, the HFB is a land facies fault basin with foreland basin sediments formatted at the Mesozoic and Cenozoic periods. The north part belongs to the south edge of the north China plate with stable sediments, and the south part changes to transitional-crust crystalline basement with slope-basin sediments at the ancient Paleozoic and Paleozoic erathem (Zhao *et al.*, 2000). For the shallow layers in the city of Hefei urban area, the major sediments are Cretaceous and Tertiary system argillaceous siltstones and fragmental rocks with varying degrees of weathering. They usually place at depths from 15 to 25 m.

To the east of the city, there exists the huge north-northeast-trending TLF zone, which has a length over 2000 km in eastern and northeastern China. The 1668 magnitude 8.5 Tancheng earthquake occurred at the TLF near Tancheng in the Shandong Province of China (red star in Fig. 1a), which is about 300 km north of Hefei. On 6 April 2009, a magnitude 3.5 earthquake occurred about 20 km northeast of the city of Hefei at the TLF zone. The earthquake caused strong-ground shaking and public concern about future earthquake hazard around the Hefei area. Since 2006, Hefei has been expanding quickly, and its population in the urban area has doubled. Therefore, the investigation of the urban subsurface structure is very useful for the simulation of earthquake strong ground motion and evaluation of engineering and architectural safety in city planning.

Because of dense population and safety issues, active source experiment is not suitable to investigate the shallow crustal structure in the urban area. However, ambient-noise cross correlation can be used to retrieve surface-wave Green's functions between receiver pairs (Shapiro and Campillo, 2004), which can be used to study 3D crustal structures with high resolution in dense array regions (e.g., Shapiro *et al.*, 2005). Surface waves

doi: 10.1785/0220150257

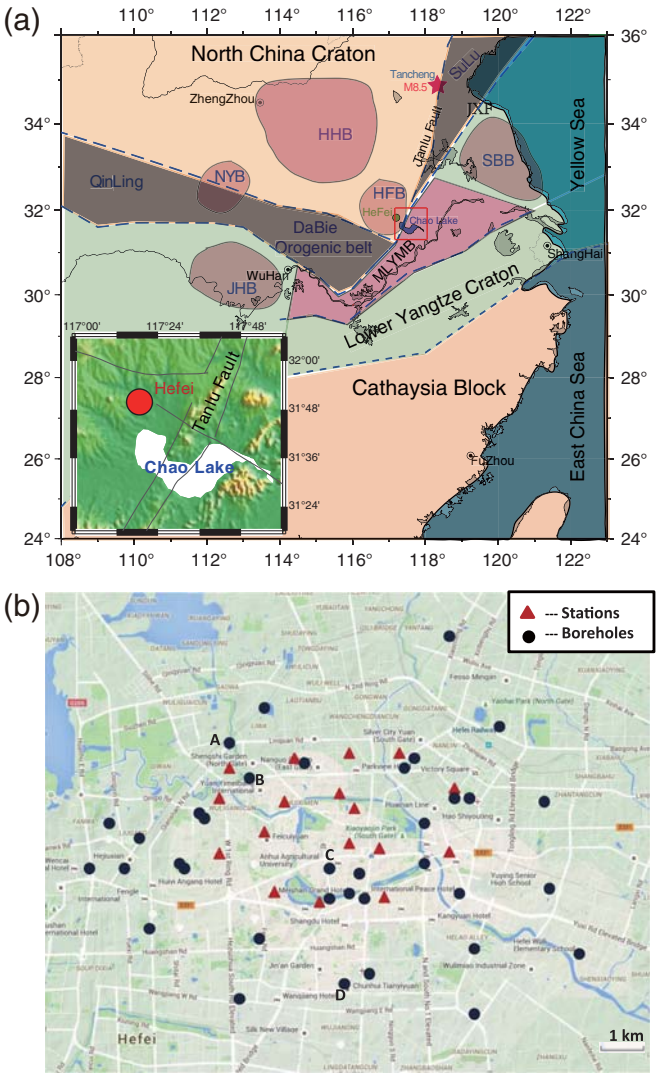

▲ **Figure 1.** (a) Location of the city of Hefei (green circle), which is in the southeast part of the Hefei basin (HFB), west of the Tanlu fault (TLF), north of Chao Lake (blue patch), and east of the Dabie orogenic belt. Other abbreviations are as follows: SBB, Sulu basin; HHB, Hehuai basin; NYB, Nanyang basin; JHB, Jianghan basin; JXF, Jiashan–Ciangshui fault; MLYMB, middle–lower Yangtze River metallic belt. The 1668 magnitude 8.5 Tancheng earthquake is shown as the red star. The lower left inset figure is an enlarged view of the region in the red rectangle on the main map, showing the topography and faults lines (in black) near the city of Hefei (red circle). (b) Distribution of seismic array stations (red triangles) and boreholes (black dots) in Hefei. The capital letters (A, B, C, and D) give the location of the borehole sites that are shown in Figure 2.

at different periods can be used to recover velocity structures at different depths. In general, high-frequency surface waves are more sensitive to shallow structure, whereas low-frequency surface waves can be used to study deeper structure.

Ambient-noise tomography in the primary (10–20 s) and the secondary (5–10 s) microseism bands is widely used to image crust structures. The primary and secondary microseisms are generated by ocean waves and their nonlinear interaction with seafloor and coastlines (e.g., Stehly *et al.*, 2006; Yang and Ritzwoler, 2008). The higher-frequency waves are usually regarded as coming from man-made sources (e.g., traffic, cultural, or human activities) and scattering from teleseismic earthquakes (Frank *et al.*, 2009; Picozzi *et al.*, 2009).

Previous studies using ambient-noise tomography method in the 5–40 s period band have already been widely used to study crust and upper mantle structure, including southern California in the United States (Shapiro *et al.*, 2005), southeastern Tibet (Yao *et al.*, 2006, 2008), Europe (Yang *et al.*, 2007), New Zealand (Lin *et al.*, 2007), and so on. Studies using higher-frequency surface waves from ambient-noise cross correlation also became popular in recent years to investigate shallow crustal or near-surface structures in small-scale regions (e.g., Picozzi *et al.*, 2009; Huang *et al.*, 2010; Pilz *et al.*, 2012; Lin *et al.*, 2013; Shirzad and Shomali, 2014; Fang *et al.*, 2015).

In this study, we collected two weeks (from 18 May to 2 June 2013) of continuous ambient-noise data from 17 stations and 36 borehole vertical velocity profiles in the city of Hefei. Then we conducted high-frequency ambient-noise tomography with constraints from these borehole data to better investigate the near-surface shear-velocity structure in the Hefei urban area.

DATA ANALYSIS AND INVERSION METHOD

Data Collection

We deployed 17 broadband stations in the urban area of the city of Hefei (Fig. 1b) with 1000 Hz sampling frequency and collected about two weeks of continuous ambient-noise recordings from 18 May to 2 June 2013 using Güralp CMG-6TD seismometers. The station coordinates are shown in Ⓔ Table S1, available in the supplement to this article. Ⓔ An example of time–frequency spectral amplitude of a one-day waveform is shown in Figure S1. The stations span an area about 5 km × 7 km, with an average spacing of about 1–2 km. The vertical component data were used for ambient-noise tomography in this study to obtain the near-surface shear-velocity structure beneath the Hefei urban city.

To get a better initial velocity model and also compare with our results from ambient-noise tomography, we collected 1D shear-velocity vertical profiles from surface to 30 m for earthquake building codes associated with site amplification estimation (Moss, 2008) from 36 boreholes in the city (black circles in Fig. 1b), which cover our research region completely. We interpolated the borehole data to obtain a 3D V_S model from surface to 30 m depth and used it as the initial model of the shallowest near surface for the later tomographic inversion. Figure 2 shows the interpolated model at three depths (0, 15, and 30 m) and four selected borehole V_S profiles. A clear velocity variation trend can be seen from Figure 2c at the depth of 30 m: high velocity in the north and low velocity in the south. From Figure 2d, shear velocity is very low (< 200 m/s) for the shallowest sediment layer (< 10 m depth) and increases quickly to about 500 m/s at a depth of 15 m for

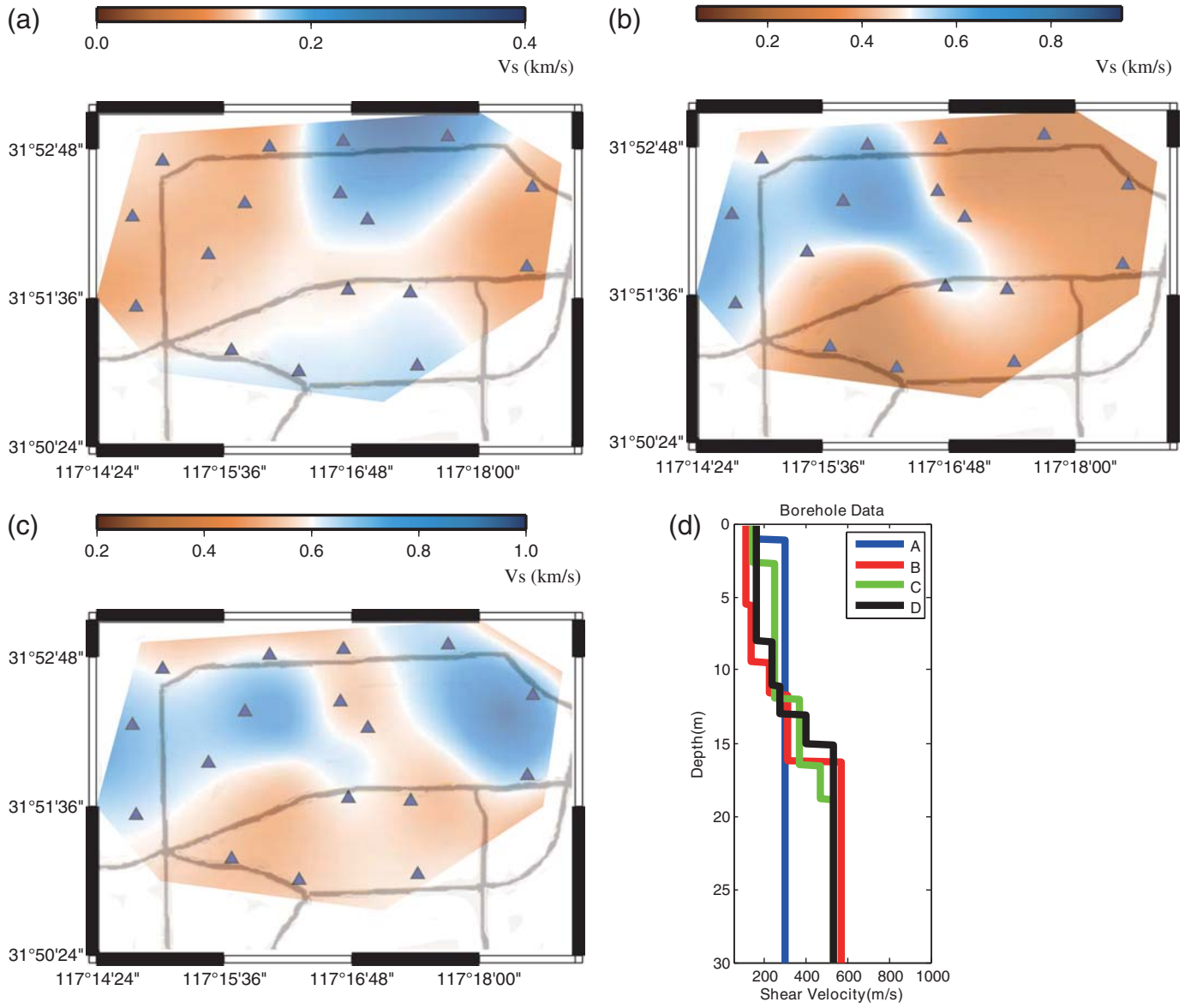

▲ **Figure 2.** The interpolated V_S model from the borehole data at three depths: (a) 0 m, (b) 15 m, and (c) 30 m. The triangles represent the array stations used in this study, and the gray lines represent some main roads in the Hefei urban area. (d) The 1D V_S profile of the four selected boreholes (A, B, C, and D) marked in Figure 1b.

the three northern borehole sites (A, B, and C in Fig. 1b). However, for borehole site D located in the south, shear velocity only reaches about 300 m/s at the depth of 30 m, which is only about half of that for northern borehole sites.

Ambient-Noise Data Processing

We prepared the vertical component data into hourly segments at a sampling rate of 100 Hz, removed the mean and trend of the data, band-pass filtered the data in the 0.5–2 s frequency band, performed spectral whitening and temporal normalization for the data (Bensen and Ritzwoller, 2007), and finally performed cross correlation to obtain the time domain cross-correlation function (CF) $C_{AB}(t)$ for the station pair A and B for each hourly data with the lag time from −50 to 50 s. All the hourly CFs from each station pair were linearly stacked together. Because of the relatively short deployment period, the signal-to-noise ratio (SNR) of stacked CFs is relatively low, although we can observe the emergence of surface-wave signals (Fig. 3a). To improve the SNR of CFs, we performed the time–frequency phase-weighted stack (Schimmel *et al.*, 2011) of the hourly CFs based on the S-transform (Stockwell *et al.*, 1996; Schimmel and Gallart, 2007) to obtain the final stacked CFs (Fig. 3b). The SNR of the retrieved surface (Rayleigh) waves from the S-transform stack method is significantly improved (Fig. 3b). One CF between an individual station pair is used to illustrate the SNR improvement, which reveals the SNR of S-transform stack method is about 27 times that of the linear stack method (Fig. 3d,e). The SNR here is

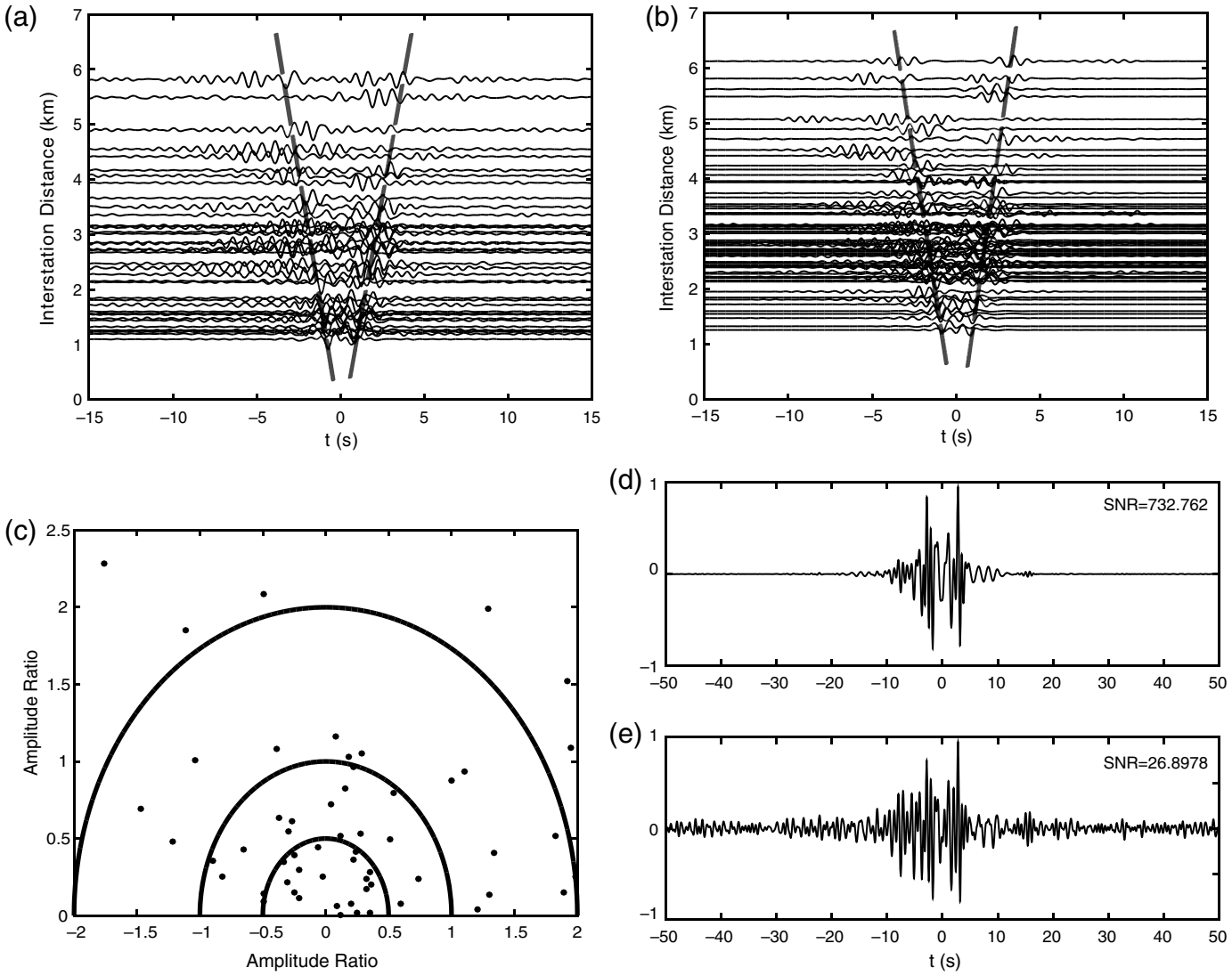

▲ **Figure 3.** Interstation cross-correlation functions (CFs) with signal-to-noise ratio (SNR) greater than five in the 0.5–2 s period band obtained from two stacking methods: (a) the conventional normalized linear stacking method (only 45 CFs) and (b) from the phase-weighted stacking method based on the S-transform (69 CFs). (c) The azimuthal distribution of the amplitude ratio (black dots) between the maximum envelope amplitudes of the positive-time and negative-time parts of a CF in (b). The azimuth of each black dot gives the azimuth direction of each station pair. (d) The stacked interstation CFs for the station pair 6h28-6h25 from the phase-weighted stacking method and (e) the conventional normalized linear stacking method.

defined as the ratio of the maximum amplitude of the signal window of CF (−25 to ∼25 s) and the average absolute amplitude of the noise window (−50 to ∼ − 25 s and 25 to ∼50 s). Meanwhile, we also compute the relative amplitude ratios of the positive and negative time CFs for all station pairs in Figure 3b to check the azimuthal distribution ambient-noise sources (Fig. 3c). If noise sources were dominated from certain directions, we would expect the relative amplitude ratios to have clear azimuthal dependence. However, this feature is not observed (Fig. 3c), so we expect the noise sources are generally distributed randomly with respect to azimuth (Fig. 3c).

The time domain empirical Green's function (TDEGF) is then derived from the time derivative of the CF (Sabra *et al.*, 2005; Yao *et al.*, 2006). We stacked the positive-time and negative-time parts of TDEGFs linearly and used the image analysis method by Yao *et al.* (2006, 2011) to extract the fundamental-mode Rayleigh-wave group and phase-velocity dispersion curves from the TDEGF of every station pair. An example of the group-velocity dispersion curve extraction is shown in Figure S2 and we do not observe high-mode surface waves or body waves in the retrieved TDEGF. We required that the interstation distance is at least 1.5 times the wavelength to approximately satisfy the far-field approximation of surface-wave propagation (Yao *et al.*, 2011). In addition, because of the flat topography in the study region, we ignored the complex effects on surface-wave propagation due to topographic variations.

All the group- and phase-velocity dispersion curves from the 0.5–2 s period (with 0.1 s interval) of the fundamental-

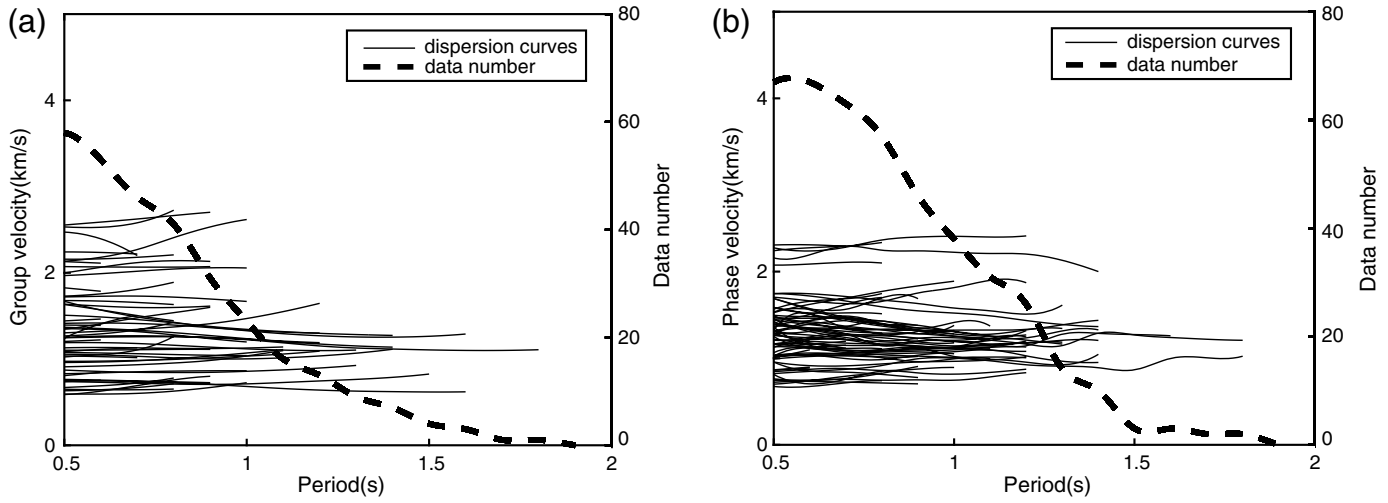

▲ **Figure 4.** (a) The group-velocity and (b) phase-velocity dispersion curves in the 0.5–2 s period band. The black solid lines represent dispersion curves, and the black dashed line represents the total number of dispersion data at each period.

mode Rayleigh waves are shown in Figure 4a and 4b, respectively. Actually the quantity of dispersion data decreases with increasing period; and, even above the 1.8 s period, no measurements can be made due to relatively short interstation distances. The velocity variation in the study region appears to be very large, as inferred from the dispersion curves. For example, at the 0.5 s period, group velocity varies from 0.5 to 2.6 km/s and phase velocity changes from 0.6 to 2.4 km/s. Finally, we obtained 735 dispersion data, including 429 phase-velocity measurements and 306 group-velocity measurements, for the next step inversion of the 3D shear-wave velocity structure in the near surface.

Inversion Method for 3D V_S Structure

In this study, we used a direct 3D surface-wave tomography method based on period-dependent raytracing to invert all dispersive travel-time data simultaneously for the 3D subsurface shear-velocity structure (Fang *et al.*, 2015). This method avoids the intermediate steps of inversion for phase- or group-velocity maps and considers raybending effects on surface-wave tomography in the complex medium. For the forward problem, the fast matching method was used to compute surface-wave travel times and ray paths between receivers and sources at each period (Rawlinson and Sambridge, 2004). The travel-time perturbation at the angular frequency ω with respect to a reference model for the path i is given by

$$\delta t_i(\omega) = t_i^{\mathrm{obs}}(\omega) - t_i(\omega) \approx -\sum_{k=1}^{K} v_{ik} \frac{\delta C_k(\omega)}{C_k^2(\omega)}, \tag{1}$$

in which $t_i^{\mathrm{obs}}(\omega)$ is the observed surface-wave travel time, $t_i(\omega)$ is the calculated travel time from a reference model that can be updated in the inversion, and v_{ik} is the bilinear interpolation coefficients along the ray path associated with the ith travel-time data and the phase (or group) velocity $C_k(\omega)$ and its perturbation $\delta C_k(\omega)$ of the kth 2D surface grid point at the angular frequency ω. Using the 1D depth kernel of Rayleigh-wave phase- or group-velocity data to compressional velocity (α), shear velocity (β), and density (ρ) at each surface grid node, we can rewrite equation (1) as

$$\begin{aligned}\delta t_i(\omega) &= \sum_{k=1}^{k}\left(-\frac{v_{ik}}{C_k^2}\right)\sum_{j=1}^{J}\left[R_\alpha'(z_j)\frac{\partial C_k}{\partial \alpha_k(z_j)}\right. \\ &\quad \left. + R_\rho'(z_j)\frac{\partial C_k}{\partial \rho_k(z_j)} + \frac{\partial C_k}{\partial \beta_k(z_j)}\right]\Bigg|_{\theta_k}\delta\beta_k(z_j) \\ &= \sum_{l=1}^{M} G_{il} m_l, \end{aligned} \tag{2}$$

in which θ_k represents the 1D reference model at the kth surface grid point on the surface and $\alpha_k(z_j)$, $\beta_k(z_j)$, and $\rho_k(z_j)$ are the compression velocity, shear velocity, and mass density at the jth depth grid node, respectively. J is the number of grid points in the depth direction, and the number of total grid points of the 3D model is $M = KJ$. We used the empirical relationships based on Brocher (2005) to relate perturbation of compressional velocity and density to perturbation of shear-wave velocity with the scaling factor $R_\alpha'(z_j)$ and $R_\rho'(z_j)$ shown in Fang *et al.* (2015).

A wavelet-based sparsity-constrained inversion (Fang and Zhang, 2014; Fang *et al.*, 2015) was used to invert for the 3D shear-wave velocity model. The multiresolution representation of wavelet transform can adaptively resolve features of different scales based on data scales (Chiao and Liang, 2003). We refer to Fang *et al.* (2015) for the details of the inversion procedures. All the measured group and phase dispersion data were incorporated into the joint inversion.

Here we used the interpolated borehole data as the initial model for the top 30 m (see Fig. 2). Because Rayleigh-wave phase velocity is most sensitive to the shear-wave velocity structure at depth around one-third of the wavelength, we also derived the 1D average shear-velocity model as the reference

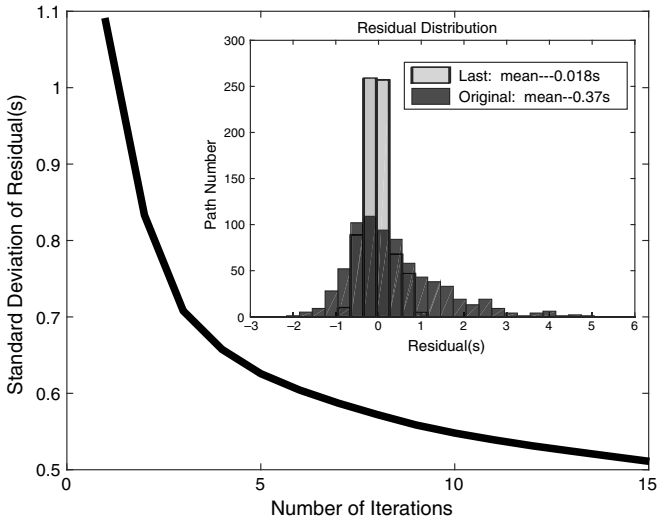

▲ **Figure 5.** Variation of the standard deviation of surface-wave travel-time residuals with the iteration number. The inset panel shows the histograms of travel-time residuals before iterations (dark gray, with a mean value about 0.37 s) and after 15 iterations (light gray with black outline, with a mean value about 0.018 s).

model below 30 m from the dispersion data using the scheme by Fang *et al.* (2015). Our inversion depth extends from 0 to 900 m. The grid spacing is 0.003° along the north–south direction and 0.005° along the east–west direction, thus giving $18 \times 18 = 256$ horizontal grid points. We set 17 grid points along the depth direction from surface to 900 m, with larger grid spacing at deeper depths.

INVERSION RESULTS

3D Shear Velocity Structure

We used both group- and phase-velocity dispersion data into the joint inversion for 3D near-surface shear-velocity structures with the borehole data as constrained in the initial model (Figs. 5–7). After inversion, the standard deviation of travel-time residuals decreases from about 1.1 s to about 0.5 s at the end (the 15th iteration; see Fig. 5). The final travel-time residuals center very well around 0 s (Fig. 5, inset panel). For comparison, we also used an initial model without borehole data to test the inversion results (Ⓔ Fig. S3). To investigate the robustness of different types of measurements, we invert for structures using only each type of datasets (Ⓔ Fig. S4).

Figure 6 shows the shear-velocity maps from the joint inversion of phase- and group-velocity dispersion data with the initial model for the top 30 m constrained by the borehole data (Fig. 2). The velocity structures are given at four depths: 30, 50, 100, and 300 m (Fig. 6a–d) and two profiles PP′ and QQ′ (Fig. 7; locations in Fig. 6b). The inversion results show that low velocities appear in the southern part and high velocities for the north part. Shear velocity is typically < 1 km/s in the southern part above 300 m depth. The deep part, for example below the depth of 300 m, has higher shear velocity, up to 2.4 km/s. At the shallow area, to the west of Xiaoyaojin Park, there is a low-velocity zone within the northern high-velocity zone (Fig. 6a). The profiles demonstrate that the velocity changes sharply at around the Changjiang Road. This trend (high velocity in the north and low velocity in the south) continues with increasing depth. The lateral velocity variation range at the same depth even increases to ∼80%.

The result agrees well with the location and geology of the study region. Hefei is located at the edge of the basin and its southern suburb close to Chao Lake (Fig. 1a). Therefore, much thicker sediments may exist south of the city that lead to very low shear velocity, as shown in Figure 6. On the contrary, the north part appears to have a much thinner sedimentary layer and more exposed bedrock that shows as high-velocity structures. The sharp lateral velocity change matches the location of the Shushan fault (SSF) very well beneath the city of Hefei, which also results in apparent gravity variation in this area (Jia *et al.*, 2002).

Path Coverage and Resolution Test

Figure 8 shows the depth sensitivity kernels for Rayleigh-wave group and phase velocities at three periods 0.5, 0.8, and 1.0 s, using the 1D velocity model at the central point of the inversion area (117.28° E, 31.861° N). It is apparent that longer-period Rayleigh waves are sensitive to deeper structure. The 0.5-s period data still have some sensitivity to the structure shallower than 100 m depth. At about 1.0 s, our dispersion data can have good sensitivity to structures about 700 m at depth.

Figure 9 shows the path coverage of phase-velocity measurements at the two selected periods (0.5 and 0.9 s) based on the final obtained 3D velocity model (Fig. 6). The path number decreases from 67 at the 0.5 s period to 14 at the 1.3 s period. The ray paths keep a good spatial coverage until the 1.0 s period, which has 40 ray paths. Because of very large velocity variations in the near surface (Fig. 6), the ray paths significantly bend off the great-circle path. The ray-path coverage, and hence the spatial resolution, will be different in the study region if we assume great-circle propagation of surface waves. From the bending direction, we can also figure out the approximate distribution of high- and low-velocity zones.

To evaluate the spatial resolution of the inversion at depths, we performed checkerboard tests with the input anomalies (Fig. 10a) following a sine function, and the amplitude range changes from −60% to 60% of the average velocity at each depth. Each anomaly has a size of 1.5 km in the north–south direction and 1.1 km in the east–west direction. Figure 10b–d shows the recovered results at three depths (100, 300, and 700 m), with the same station and path distribution as shown in Figure 9. The checkerboard pattern is well resolved in the center of the study region. The resolution is much better at the shallower depths of 100 and 300 m than at 700 m due to the much smaller quantity of dispersion data above 1.0 s.

DISCUSSION

In this study, we used the high-frequency ambient-noise tomography to reveal near-surface velocity structure in the urban area

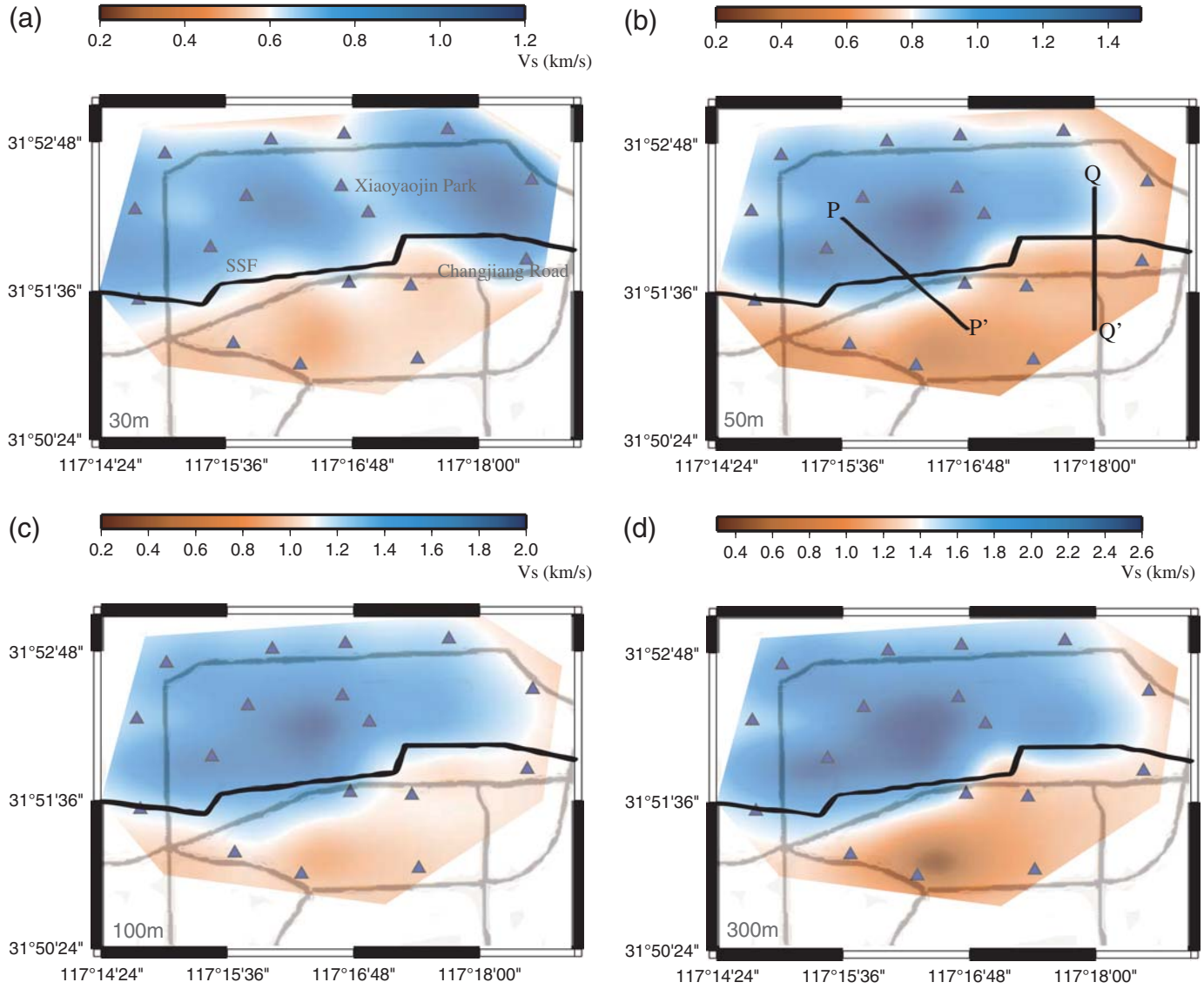

▲ **Figure 6.** The final V_S model obtained from the joint inversion. (a–d) give the V_S structure at four depths, 30, 50, 100, and 300 m, respectively. The triangles represent the stations. The solid black line represents the Shushan fault (SSF). The gray lines represent the main road in the city. The two black straight lines PP′ and QQ′ in (b) represent the two profiles in Figure 7.

of the city of Hefei in eastern China. Because the data collection time for the temporary array is only two weeks, the S-transform-based phase-weighted stacking method was used to enhance the SNR of the retrieved surface-wave signals. Because of strong attenuation of high-frequency waves, much shorter interstation distances (for instance, a few kilometers in this study) are better for recovering the high-frequency (~1 Hz or higher) surface-wave Green's functions from ambient-noise cross correlation. Generally speaking, the shorter the interstation distance is, the higher the frequency of the recovered signal can reach. Meanwhile, sufficient ambient-noise sources are also necessary for convergence of the retrieved signals. In the urban area, human activities, such as moving vehicles, are regarded as the main noise sources for high-frequency signals. Two weeks of data for this study are barely enough to recover surface-wave signals with good SNR. However, the number of days of continuous data for obtaining stable high-frequency empirical Green's functions may depend on the actual situation. In addition, we find obvious temporal changes of noise sources caused by human activities in the data (Ⓔ Fig. S1). During the night (00:00–05:00 Beijing local time), the spectrum amplitude for frequencies > 1.2 Hz decreases compared with other times during the day, but the spectrum amplitude does not seem to be greatly affected in the 0.5–1.2 Hz frequency band. The recovery of high-frequency surface waves does need closer station spacing due to stronger attenuation.

Because of large variations of dispersion measurements in this study (Fig. 4), we expect strong off-great-circle propagation of high-frequency surface waves. This large structural variation in near-surface shear-velocity structures is also evident from

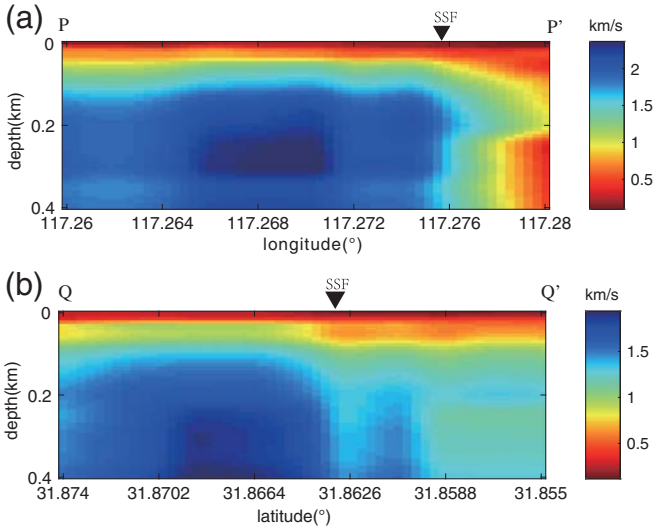

▲ **Figure 7.** Two V_S profiles (a) PP′ and (b) QQ′ with the locations marked in Figure 1b. The black inverted triangles represent the location of the SSF.

borehole data (Fig. 2). Therefore, it is not appropriate to use the assumption of great-circle propagation of surface waves that is used in most ambient-noise tomography. Some studies (e.g., Young *et al.*, 2011) performed ambient-noise phase-velocity tomography with consideration of the raybending effect at high frequencies. Others (e.g., Lin *et al.*, 2009; Gouédard *et al.*, 2012) used the eikonal tomography approach to directly estimate the phase-velocity variations in dense array regions, which inherently considers the raybending effect based on surface-wave travel-time observations. In our study, the array only consists of 17 stations, so we adopted the direct 3D shear-velocity inversion method from dispersion data (Fang *et al.*, 2015) based on frequency-dependent raytracing (Rawlinson and Sambridge, 2004). This method does not need to generate 2D phase- or group-velocity maps at each period, but directly inverts all path-dependent and frequency-dependent surface-wave travel-time measurements for 3D shear-velocity structures. However, it computes the ray paths at each period based on the phase-velocity maps derived from the 3D model, which is updated at each iteration step in the inversion. For contrast, we also perform the joint inversion following the great-circle assumption of surface-wave propagation (Ⓔ Figs. S5 and S6). However, the results are much different from those based on surface-wave raytracing (Figs. 6 and 7) and cannot resolve the sharp velocity changes around the SSF.

From the joint inversion results (Fig. 6), the north part generally presents high velocities and the south part shows low velocities. The shape of the transition area between the high-velocity zone and the low-velocity zone also involves some changes at 50, 100, and 300 m depths. It seems that the high-velocity zone in the north part changes sharply at the transition zone along the profile PP′, whereas the change is more gradual along the profile QQ′. There also exists a relative low-velocity zone at very shallow depths (30 and 50 m; see Fig. 6a,b) between the high-velocity regions in the northern part. As seen from the supplementary material (Ⓔ Fig. S3), this low-velocity area in the northern part does not exist if we do not use the borehole data as the initial velocity model in the top 30 m. Therefore, this low-velocity region at 30 and 50 m is probably due to the initial constraints from the borehole data at the top 30 m (Fig. 2c).

The city of Hefei is just adjacent to the TLF and has significant potential for earthquake hazards in the future. Our ambient-noise tomography reveals large velocity variations of the near-surface structures beneath the city of Hefei, which can be used to predict strong ground motion and to assess po-

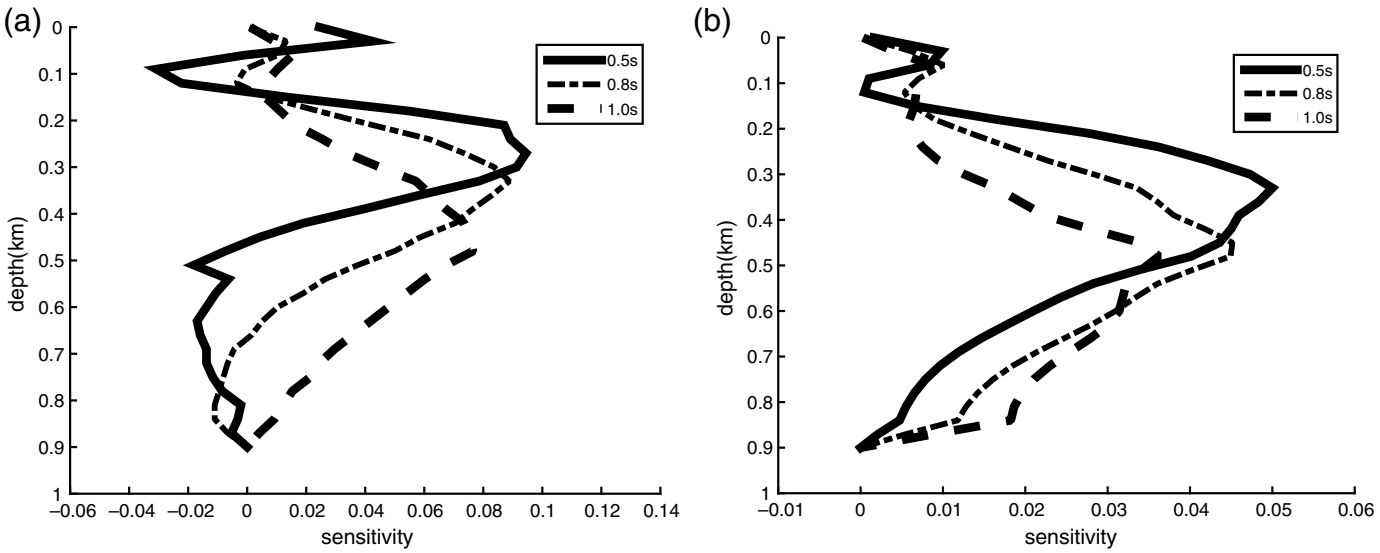

▲ **Figure 8.** Depth sensitivity kernels for (a) group velocity and (b) phase velocity at three periods: 0.5 s (solid line), 0.8 s (dotted line), and 1.0 s (dashed line).

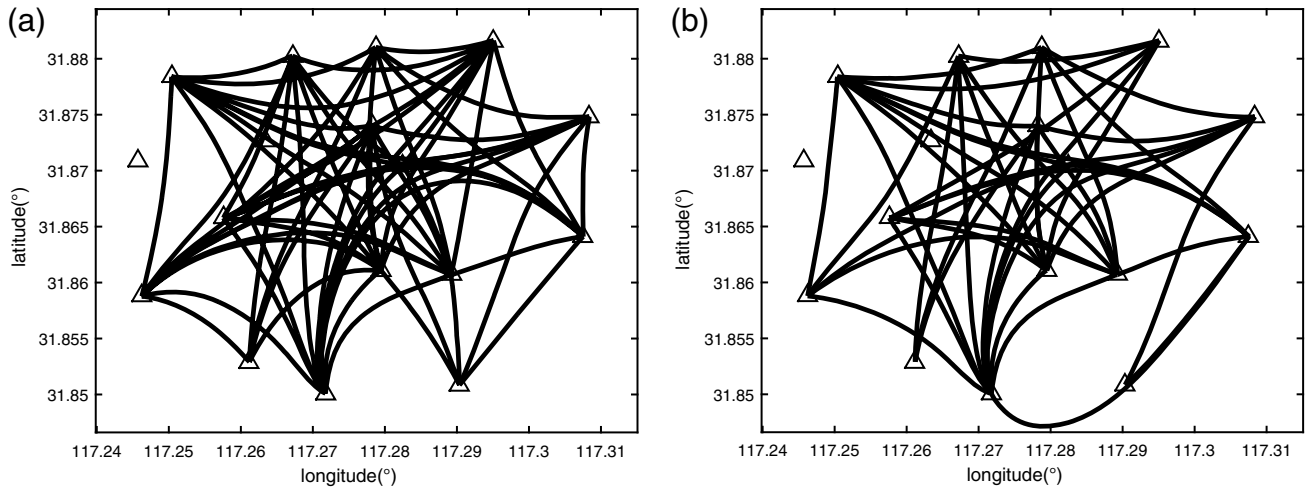

▲ **Figure 9.** Ray-path coverage for the two selected periods: (a) 0.5 s and (b) 0.9 s. The black lines represent the ray paths and the triangles represent the stations.

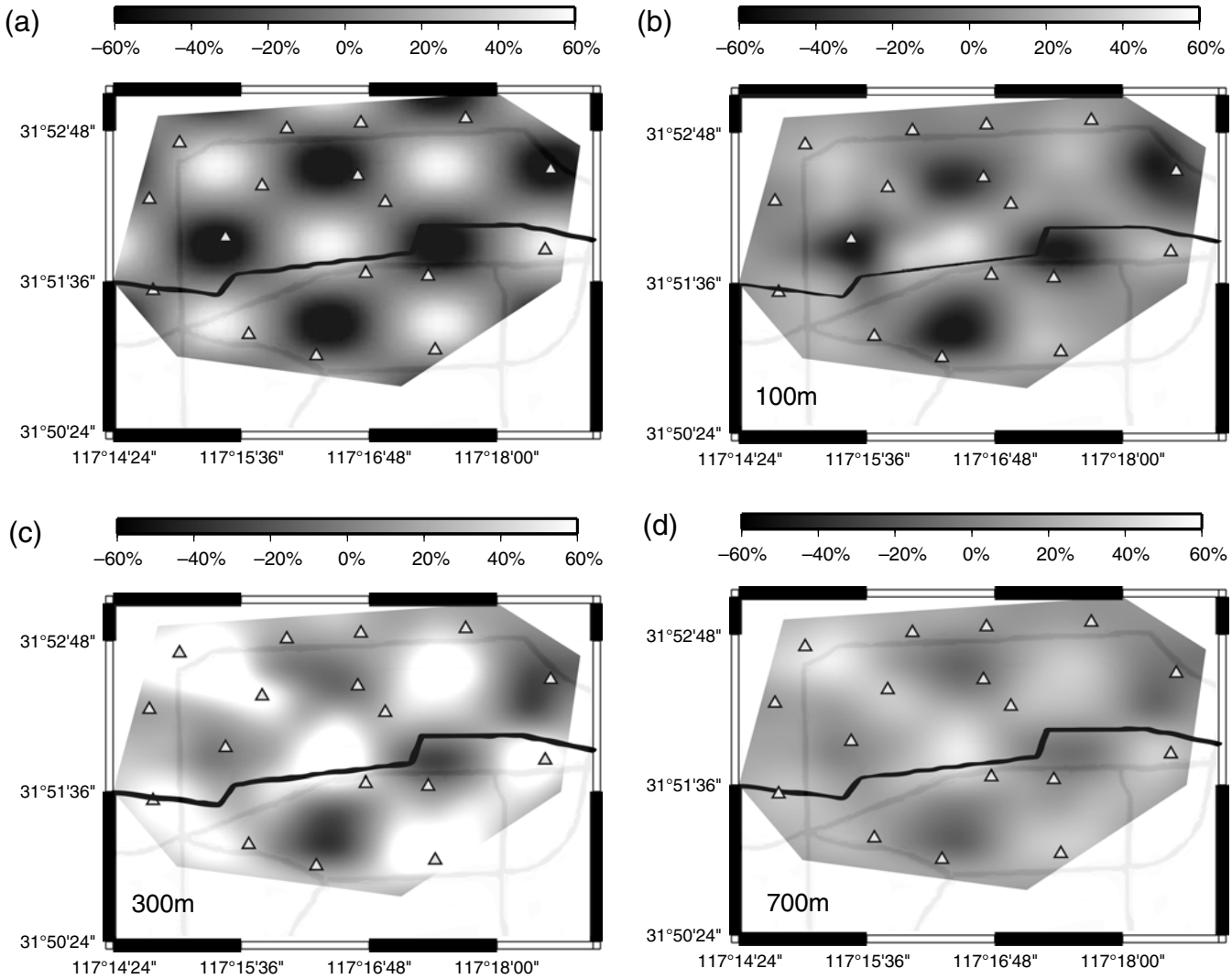

▲ **Figure 10.** Checkerboard resolution tests of the inversion results: (a) the input checkerboard model and (b–d) the recovered checkerboard model at depths 100, 300, and 700 m, respectively.

tential seismic hazards in the future. Typical borehole velocity analysis for earthquake engineering purposes only reaches 30 m underground. However, with high-frequency ambient-noise tomography, we extend the depth of velocity structure to several hundred meters, which is important for designing tall skyscrapers, subway systems, and some other large underground structures. Therefore, our study is useful for future city planning and is of strong engineering interest in the future. Because of the limited array size, this study can only resolve the structure in the top ~400 m from ambient-noise tomography. Future studies with a large array size may help to obtain the shallow crustal structure in the top several kilometers, such as for the Taipei basin study, which uses an array of approximately 10 km × 10 km (Huang *et al.*, 2010; Fang *et al.*, 2015).

CONCLUSION

This study used high-frequency ambient-noise tomography with constraints from shallow borehole data to investigate the near-surface shear-velocity structures of the Hefei urban area. We extracted high-frequency fundamental-mode Rayleigh-wave signals from ambient-noise cross correlation of two weeks data in the 0.5–2 s period band. The nonlinear phase-weighted stacking method based on the S-transform was used to improve the SNR of the recovered surface-wave signals. We used a direct surface-wave inversion method that simultaneously inverts all phase- and group-velocity dispersion data for 3D variations in shear-velocity structures in the top ~400 m. Our results reveal very large velocity variations in the near surface of the study region. The north part of the city of Hefei shows high shear-velocity structures, whereas the south part, which is closer to Chao Lake, shows very low shear-velocity structures due to much thicker sediments. The sharp velocity variation matches the location of SSF very well. Our results agree well with the local geology and are useful for predicting strong ground motion and potential seismic hazards of the city of Hefei.

DATA AND RESOURCES

The data collected in this project are currently managed by Huajian Yao, and any collaborative work with this dataset is welcome. The direct inversion package of surface-wave dispersion data for 3D V_S structure is also available to other researchers. For those interested in the dataset and software package, please e-mail Huajian Yao (hjyao@ustc.edu.cn).

ACKNOWLEDGMENTS

We thank the Editor Zhigang Peng and two anonymous reviewers for constructive comments that helped to improve the original manuscript. We acknowledge M. Schimmel for providing us the S-transform-based phase-weighted stacking code. We also thank Longbin Ouyang for providing the basic tectonic map used in this paper (Fig. 1a). This research is supported by the National Natural Science Foundation of China (Grant Number 41222028), China National Special Fund for Earthquake Scientific Research in Public Interest (Grant Number 201508008), and the Fundamental Research Funds for the Central Universities (Grant Number WK2080000053).

REFERENCES

Bensen, G. D., and M. H. Ritzwoller (2007). Processing seismic ambient noise data to obtain reliable broad-band surface wave dispersion measurements, *Geophys. J. Int.* **169,** 1239–1260, doi: 10.1111/j.1365-246X.2007.03374.x.

Brocher, T. M. (2005). Empirical relations between elastic wavespeeds and density in the Earth's crust, *Bull. Seismol. Soc. Am.* **95,** no. 6, 2081–2092.

Chiao, L.-Y., and W.-T. Liang (2003). Multiresolution parameterization for geophysical inverse problems, *Geophysics* **68,** no. 1, 199–209.

Ding, L., Z. Liu, M. Lei, and L. Pei (2002). Structural styles and evolution in the Hefei basin, *Petrol. Geol. Exp.* **24,** no. 3, 204–208.

Fang, H., and H. Zhang (2014). Wavelet-based double-difference seismic tomography with sparsity regularization, *Geophys. J. Int.* **199,** no. 2, 944–955.

Fang, H., H. Yao, H. J. Zhang, Y.-C. Huang, and R. D. van der Hilst (2015). Direct inversion of surface wave dispersion for three-dimensional shallow crustal structure based on ray tracing: Methodology and application, *Geophys. J. Int.* **201,** no. 3, 1251–1263, doi: 10.1093/gji/ggv080.

Frank, S. D., A. E. Foster, A. N. Ferris, and M. Johnson (2009). Frequency dependent asymmetry of seismic cross-correlation functions associated with noise directionality, *Bull. Seismol. Soc. Am.* **99,** 462–470.

Gouédard, P., H. Yao, F. Ernst, and R. D. van der Hilst (2012). Surface wave eikonal tomography in heterogeneous media using exploration data, *Geophys. J. Int.* **191,** no. 2, 781–788, doi: 10.1111/j.1365-246X.2012.05652.x.

Huang, Y.-C., H. Yao, B.-S. Huang, R. D. van der Hilst, K.-L. Wen, W.-G. Huang, and C.-H. Chen (2010). Phase velocity variation at periods 0.5–3 s in the Taipei basin of Taiwan from correlation of ambient seismic noise, *Bull. Seismol. Soc. Am.* **100,** no. 5A, 2250–2263.

Jia, H. Y., X. X. Lv, Y. P. Li, H. J. Yan, J. S. Hu, G. H. Liu, and Y. Y. Zhang (2002). The characteristics of gravity field in Hefei basin, *Petrol. Geol. Exp.* **24,** no. 3, 232–242.

Lin, F.-C., D. Li, R. W. Clayton, and D. Hollis (2013). High-resolution 3D shallow crustal structure in Long Beach, California: Application of ambient noise tomography on a dense seismic array, *Geophysics* **78,** no. 4, Q45–Q56.

Lin, F. C., M. H. Ritzwoller, J. Townend, S. Bannister, and M. K. Savage (2007). Ambient noise Rayleigh wave tomography of New Zealand, *Geophys. J. Int.* **170,** 649–666.

Lin, F.-C., M. H. Ritzwoller, and R. Snieder (2009). Eikonal Tomography: Surface wave tomography by phase-front tracking across a regional broad-band seismic array, *Geophys. J. Int.* **177,** no. 3, 1091–1110, doi: 10.1111/j.1365-246X.2009.04105.x.

Moss, R. E. S. (2008). Quantifying measurement uncertainty of thirty-meter shear-wave velocity, *Bull. Seismol. Soc. Am.* **98,** 1399–1411.

Picozzi, M., S. Parolai, D. Bindi, and A Strollo (2009). Characterization of shallow geology by high-frequency seismic noise tomography, *Geophys. J. Int.* **176,** 164–174.

Pilz, M., S. Parolai, M. Picozzi, and D. Bindi (2012). Three-dimensional shear wave velocity imaging by ambient seismic noise tomography, *Geophys. J. Int.* **189,** no. 1, 501–512.

Rawlinson, N., and M. Sambridge (2004). Wave front evolution in strongly heterogeneous layered media using the fast marching method, *Geophys. J. Int.* **156,** no. 3, 631–647.

Sabra, K. G., P. Gerstoft, P. Roux, W. A. Kuperman, and M. C. Fehler (2005). Extracting time-domain Green's function estimates from ambient seismic noise, *Geophys. Res. Lett.* **32,** L03310, doi: 10.1029/2004GL021862.

Schimmel, M., and J. Gallart (2007). Frequency-dependent phase coherence for noise suppression in seismic array data, *J. Geophys. Res.* **112,** no. B04303, doi: 10.1029/2006JB004680.
Schimmel, M., E. Stutzmann, and J. Gallart (2011). Using instantaneous phase coherence for signal extraction from ambient noise data at a local to a global scale, *Geophys. J. Int.* **184,** 494–506.
Shapiro, N. M., and M Campillo (2004). Emergence of broadband Rayleigh waves from correlations of the ambient seismic noise, *Geophys. Res. Lett.* **31,** L07614, doi: 10.1029/2004GL019491.
Shapiro, N. M., M. Camplillo, L. Stehly, and M. H. Ritzwoller (2005). High-resolution surface-wave tomography from ambient seismic noise, *Science* **307,** no. 5715, 1615–1618, doi: 10.1126/science.1108339.
Shirzad, T., and Z. H. Shomali (2014). Shallow crustal structures of the Tehran basin in Iran resolved by ambient noise tomography, *Geophys. J. Int.* **196,** no. 2, 1162–1176.
Stehly, L., M. Campillo, and N Shapiro (2006). A study of seismic noise from its long-range correlation properties, *J. Geophys. Res.* **111,** no. B10306, doi: 10.1029/2005JB004237.
Stockwell, R. G., L. Mansinha, and R. P. Lowe (1996). Localization of the complex spectrum: The S transform, *IEEE Trans. Signal Process.* **44,** no. 4, 998–1001.
Yang, Y., and M. H Ritzwoller (2008). The characteristics of ambient seismic noise as a source for surface wave tomography, *Geochem. Geophys. Geosys.* **9,** no. 2, Q02008, doi: 10.1029/2007GC001814.
Yang, Y., M. H. Ritzwoller, A. L. Levshin, and N. M. Shapiro (2007). Ambient noise Rayleigh wave tomography across Europe, *Geophys. J. Int.* **168,** 259–274.
Yao, H., C. Beghein, and R. D. van der Hilst (2008). Surface wave array tomography in SE Tibet from ambient seismic noise and two-station analysis—II. Crustal and upper-mantle structure, *Geophys. J. Int.* **173,** no. 1, 205–219, doi: 10.1111/j.1365-246X.2007.03696.x.
Yao, H., P. Gouédard, J. McGuire, J. Collins, and R. D. van der Hilst (2011). Structure of young East Pacific Rise lithosphere from ambient noise correlation analysis of fundamental- and higher-mode Scholte-Rayleigh waves, *C. R. Geoscience* **343,** 571–583, doi: 10.1016/j.crte.2011.04.004.
Yao, H., R. D. van der Hilst, and M. V. De Hoop (2006). Surface-wave array tomography in SE Tibet from ambient seismic noise and two-station analysis—I. Phase velocity maps, *Geophys. J. Int.* **166,** 732–744.
Young, M. K., N. Rawlinson, P. Arroucau, A. M. Reading, and H. Tkalčić (2011). High-frequency ambient noise tomography of southeast Australia: New constraints on Tasmania's tectonic past, *Geophys. Res. Lett.* **38,** L13313, doi: 10.1029/2011GL047971.
Zhao, Z., S. Yang, H. Chen, G. Zhu, and J. Zhou (2000). Tectonic attribute of basement in Hefei basin, Anhui Province, China, *Scientia Geologica China* **35,** no. 3, 288–296.

Cheng Li[1]
Huajian Yao[1]
Hongjian Fang[1]
Kesong Wan[1]
Haijiang Zhang[1]
Laboratory of Seismology and Physics of Earth's Interior
School of Earth and Space Sciences
University of Science and Technology of China
Hefei 230026, China
hjyao@ustc.edu.cn

Xianliang Huang
Institute of Engineering
Earthquake Administration of Anhui Province
Hefei 230031, China

Kangdong Wang[2]
Geological Survey of Anhui Province
Hefei 230001, China

Published Online 18 May 2016

[1] Also at National Geophysical Observatory, Mengcheng, Bozhou, Anhui 233527, China.
[2] Also at Laboratory of Seismology and Physics of Earth's Interior, School of Earth and Space Sciences, University of Science and Technology of China, Hefei 230026, China.